Optimizing a Human Monoclonal Antibody for Better Neutralization of SARS-CoV-2

Qian Wang[1,2,3,9], Yicheng Guo[1,3,9], Ryan G. Casner[4,5,6,9], Jian Yu[1], Manoj S. Nair[1], Jerren Ho[1], Eswar R. Reddem[4,5], Ian A. Mellis[1], Madeline Wu[1], Chih Chen Tzang[1], Hsiang Hong[1], Yaoxing Huang[1,2,3], Lawrence Shapiro[1,4,5,*], Lihong Liu[1,3,7,*], David D. Ho[1,2,3,8,*]

[1]Aaron Diamond AIDS Research Center, Columbia University Vagelos College of Physicians and Surgeons, New York, NY 10032, USA

[2]Pandemic Research Alliance unit at the Wu Center for Pandemic Research, Columbia University Vagelos College of Physicians and Surgeons, New York, NY 10032, USA

[3]Division of Infectious Diseases, Department of Medicine, Columbia University Vagelos College of Physicians and Surgeons, New York, NY 10032, USA

[4]Zuckerman Mind Brain Behavior Institute, Columbia University, New York, NY 10027, USA

[5]Department of Biochemistry and Molecular Biophysics, Columbia University Vagelos College of Physicians and Surgeons, New York, NY 10032, USA

[6]Current address: Large Molecules Research, Sanofi R&D, Cambridge, MA 02141, USA

[7]Current address: State Key Laboratory of Virology and Taikang Center for Life and Medical Sciences, Wuhan University, Wuhan, Hubei, 430072, China

[8]Department of Microbiology and Immunology, Columbia University Vagelos College of Physicians and Surgeons, New York, NY 10032, USA

[9]These authors contributed equally

*Correspondence: lss8@cumc.columbia.edu (L.S.), ll3411@cumc.columbia.edu, (L.L.), dh2994@cumc.columbia.edu (D.D.H.)

Abstract

SARS-CoV-2 has largely evolved to resist antibody pressure, with each successive viral variant becoming more and more resistant to serum antibodies in the population. This evolution renders all previously authorized anti-spike therapeutic monoclonal antibodies inactive, and it threatens the remaining pipelines against COVID-19. We report herein the isolation of a human monoclonal antibody with a broad but incomplete SARS-CoV-2 neutralization profile, but structural analyses and mutational scanning lead to the engineering of variants that result in greater antibody flexibility while binding to the viral spike. Three such optimized monoclonal antibodies neutralize all SARS-CoV-2 strains tested with much improved potency and breadth, including against subvariants XEC and LP.8.1. The findings of this study not only present antibody candidates for clinical development against COVID-19, but also introduce a unique engineering approach to improve antibody activity via increasing conformational flexibility.

Keywords: SARS-CoV-2, COVID-19, JN.1 sublineages, monoclonal antibodies, antibody engineering, virus neutralization, viral evolution, mutational scanning, conformational flexibility, VH3-53/66, cryo-EM, and escape mutations.

Introduction

Since the emergence of COVID-19 in late 2019, its causative agent, SARS-CoV-2, has undergone considerable evolution driven by immune pressure, with each successive viral variant becoming more resistant to serum antibodies elicited by prior infection and/or vaccination. By late 2020, mutations in the viral spike protein resulted in a discernible antigenic drift that yielded the Alpha variant, which evaded antibodies targeting the antigenic supersite on the N-terminal domain (NTD)[1-3]. Shortly thereafter, further antigenic drift led to the Beta and Gamma variants that evaded not only NTD-directed antibodies but also some antibodies directed to so-called class 1 and class 2 regions of the receptor-binding domain (RBD)[1, 4, 5]. These variants were in turn rapidly replaced by the Delta variant that dominated much of 2021, and it evaded antibodies directed to select class 2 and class 3 epitopes on the RBD[6]. Importantly, this initial wave of SARS-CoV-2 variants knocked out three therapeutic monoclonal antibodies (mAbs) authorized to treat COVID-19 infection – etesevimab, bamlanivimab, and casirvimab[6-10].

The first major SARS-CoV-2 antigenic shift occurred with emergence of the Omicron (BA.1) variant in late 2021 in southern Africa[11, 12], likely due to a saltatory event resulting in an accumulation of 34 spike mutations. This variant rapidly gained dominance in the population, as a consequence of its exceptional resistance to serum antibodies in the population[13-18]. Specifically, mutations in Omicron impaired the neutralizing activity of antibodies targeting all regions (classes 1-4) of the RBD, as well as two additional clinically authorized mAbs – imdevimab and tixagevimab[9, 13, 19]. Antigenic drift from BA.1 then ensued successively throughout 2022 and yielded subvariants BA.2, BA.5, and BQ.1.1, each being more antibody resistant than its predecessor. This evolutionary drift also knocked out the utility of three more clinically authorized mAbs – sotrovimab, ciligavimab, and bebtelovimab[19-23].

The second major antigenic shift was detected in late 2022 when a recombination event between BA.2 and BA.2.75 resulted in the XBB subvariant, which promptly evolved into XBB.1.5, EG.5.1, HK.3, and HV.1 via further antigenic drift[11, 24-26]. Again, each progeny subvariant was more antibody resistant than its predecessor, largely by evading more antibodies directed to the class 1 region of RBD. Sequentially, these subvariants dominated much of 2023 until the third major antigenic shift led to the emergence of BA.2.86, which presumably was due to another saltatory event, again in southern Africa, leading to an accumulation of >30 mutations in the BA.2 spike[27]. This new subvariant was again highly resistant to serum neutralizing antibodies, including those targeting the subdomain 1 (SD-1) region of spike[28-30]. With one additional spike mutation, L455S, BA.2.86 became JN.1, and the JN.1 sublineage has been dominant worldwide from late 2023 until recently[31, 32].

In March 2024, a monoclonal antibody known as pemivibart (VYD222) was authorized for clinical use as pre-exposure prophylaxis for immunocompromised individuals who do not respond robustly to COVID-19 vaccines[33]. This antibody was specifically engineered to have broad activity against many known SARS-CoV-2 strains, including JN.1. However, as the JN.1 sublineage continued its antigenic drift, new forms such as XEC began to replace their

predecessor in recent months. As of April 2025, the dominant SARS-CoV-2 strians are XEC and LP.8.1[34]. Alarmingly, these subvariants are already ~18-28-fold more resistant to pemivibart *in vitro* than JN.1[35, 36]. This looming threat to the only authorized pre-exposure prophylaxis for millions of immunocompromised individuals who live in fear of COVID-19 is a stark reminder of the necessity to continue to develop more medical interventions to keep up with SARS-CoV-2 evolution. In addition, another mAb, AstraZeneca's sipavibart (AZD3152), is also in clinical trials; however, this antibody has been shown to be affected by the F456L mutation[37], which is present in multiple dominant JN.1 sublineages, such as XEC and LP.8.1.

We now describe the isolation and characterization of a human monoclonal antibody, 19-77, with a broad but incomplete SARS-CoV-2 neutralization profile. Structural analyses and mutational scanning led to the construction of engineered antibody variants, 19-77Δ, with a single amino-acid substitution at residue R71 in the framework region 3 of the heavy chain. These modifications resulted in greater flexibility of the complementarity-determining regions (CDRs) of the heavy chain while binding to the viral spike, thereby enabling three 19-77Δ variants to neutralize all SARS-CoV-2 strains tested with much improved potency and breadth, including against the prevalent JN.1 sublineages today. The findings of this study not only offer new antibody candidates for pre-exposure prophylaxis against COVID-19 for immunocompromised individuals, but also introduce a unique engineering approach to improve antibody activity.

Results

Isolation and characterization of mAb 19-77

To isolate new neutralizing mAbs against SARS-CoV-2, we studied Donor 19 who had been infected by the Omicron BA.5 subvariant despite having received three doses of the original monovalent vaccine (BNT162b2) and one dose of the WT/BA.5 bivalent vaccine (mRNA-1273.222) (**Extended Data Fig. 1a**). His serum, obtained ~7 months after breakthrough infection, strongly neutralized the D614G strain but less potently against XBB.1.5 and SARS-CoV (**Extended Data Fig 1b**). Given the dominance of XBB.1.5 at the start of this study, XBB.1.5 and SARS-CoV spikes were used as probes to sort antigen-specific memory B cells from his peripheral blood mononuclear cells (PBMCs). The proportions of his antigen-specific B cells were 0.16% for XBB.1.5 spike, 0.067% for SARS-CoV, and 0.12% for both XBB.1.5 and SARS-CoV spikes; in contrast, PBMCs from two healthy donors showed negligible antigen-specific B cells (**Extended Data Fig. 1c**).

Donor 19's memory B cells from quadrants 2 and 3 (**Extended Data Fig. 1c**) were then subjected to single-cell RNA sequencing using 10X Genomics to obtain paired heavy and light chain sequences of each B cell receptor, as previously described[38]. A total of 113 paired sequences were selected, and the corresponding antibodies were synthesized for *in vitro* characterization. A majority (75) of the mAbs bound the D614G spike at a concentration of 10 μg/ml, but only 29 neutralized either D614G or EG.5.1 *in vitro* (**Extended Data Fig. 1d**). Among the neutralizing mAbs, 19-77 was chosen for further studies, because it not only bound strongly to the D614G spike and RBD by immunoassays (**Fig. 1a**), but also showed broadly neutralizing activity against many SARS-CoV-2 strains (**Fig. 1b**). Specifically, in pseudovirus assays, 19-77 neutralized D614G, Alpha, Beta, Gamma, Delta, BA.1, BA.2, BA.5, BQ.1.1, XBB.1.5, EG.5.1, BA.2.86, and JN.1 with IC_{50} values <0.05 μg/ml. However, its neutralizing activity was lower against HK.3 and JF.1, and not detectable against JD.1.1 or SARS-CoV.

Genetic analysis revealed that the heavy chain of 19-77 utilized IGHV3-53 (**Extended Data Fig. 1e**), showing that this antibody belonged to the well-studied VH3-53/66 class of antibodies targeting the SARS-CoV-2 spike. Its light chain originated from IGKV3-11. Notably, the CDRH3 of 19-77 contained only 9 amino acids, one of the shortest among published VH3-53/66 class mAbs (**Fig. 1c**). Moreover, the level of somatic hypermutation of its heavy chain was the highest observed among VH3-53/66 mAbs, and its light chain was also quite hypermutated (**Fig. 1c**). These striking genetic features demonstrated the uniqueness of 19-77 and prompted further studies.

To understand the molecular basis for the neutralization breadth and potency of 19-77, we then visualized its Fab fragment in complex with the D614G spike (**Fig. 1d, Extended Data Fig. 2 and Extended Data Fig. 3a-b**) by single-particle cryo-electron microscopy (cryo-EM). The Fab was predominantly bound to the spike protein in a three-RBD-up conformation, like other VH3-53/66 class antibodies targeting the class 1 region[39]. The primary interaction between the 19-77 heavy chain and the RBD was mediated by CDRH1 and CDRH2, with hydrogen bonds

153 to A475, N487, Y473, D420, and Y421 (**Fig. 1e**). The CDRH3 region formed two hydrogen
154 bonds with the RBD: one between R97 and the backbone carbonyl of N487, and another
155 between E102 and Y489. On the other hand, the 19-77 light chain made contacts with the
156 apical ridge of the RBD via its CDRL1 and CDRL3 (**Fig. 1f**).
157
158 **Structural explanation for the loss of 19-77 activity against certain Omicron subvariants**
159
160 The antibody footprint of 19-77 on the RBD largely overlapped with the human ACE2 receptor
161 binding site (**Fig. 2a**). Sequence conservation analysis indicated that most regions of its epitope
162 are relatively conserved, except for the upper half of the left shoulder, which exhibits
163 significant sequence variations at positions 455, 456, 475, 478, and 486. These specific
164 residues have undergone frequent mutations in certain recent subvariants, such as EG.5.1,
165 HK.3, JF.1, and JD.1.1. It is therefore not surprising that the neutralizing activity of 19-77
166 against HK.3 (XBB.1.9.2 carrying Q52H and L455F/F456L mutations) and JF.1 (XBB.1.16.6
167 carrying E180V, L455F/F456L, and K478R) decreased by 14- and 42-fold, respectively,
168 compared with that against XBB.1.5 (**Fig. 1b**). The inactivity of 19-77 against JD.1.1 is likely
169 due to its A475V mutation that causes a steric clash with CDRH1 (**Fig. 2b**). To further
170 understand the resistance mechanism of L455F/F456L mutations to the neutralization by 19-
171 77, we determined the structure of 19-77 Fab in complex with the RBD of EG.5.1 by X-ray
172 crystallography, as well as the cryo-EM structures of the D614G RBD and the HK.3 RBD in
173 complex with the Fabs of 19-77 and S309 (sotrovimab) (**Extended Data Fig. 3**), a non-
174 overlapping mAb used to increase the molecular mass for visualization by cryo-EM.
175 Compared with the D614G RBD (**Fig. 2c**), the change from phenylalanine (F) to leucine (L) at
176 residue 456 in the EG.5.1 RBD reduced hydrophobic interactions with $P100_{HC}$ in the CDRH3
177 of 19-77 (**Fig. 2d**). Additionally, the L455F mutation in HK.3 introduced a minor van der
178 Waals clash with $P100_{HC}$ (**Fig. 2e**).
179
180 **Optimization of 19-77**
181
182 Given the minor to moderate steric clashes between the RBDs of resistant viruses and 19-77,
183 we explored the possibility of optimizing the antibody to accommodate for the resistance
184 mutations. Utilizing *in-silico* modeling and the energy-calculation algorithm FoldX[40], we
185 performed saturation mutagenesis on each residue of both the heavy and light chain, comparing
186 the binding energy changes ($\Delta\Delta G$) between each mutant and the original 19-77 in complex
187 with the HK.3 RBD that contained the L455F/F456L mutations. Both beneficial and
188 detrimental mutations were identified (**Extended Data Fig. 4a**; data for light chain not shown).
189 Interestingly, substitutions at residue R71 in framework region 3 of the heavy chain
190 consistently predicted a moderately beneficial effect (~0.5 kcal/mol) on the binding of 19-77
191 to the HK.3 RBD. We then conducted alanine scanning on the antigen-contact residues of both
192 heavy and light chains of 19-77, in addition to the residue R71, followed by testing each
193 modified antibody for neutralization against JD.1.1, HK.3, EG.5, and EG.5-A475V (**Fig. 3a,**
194 **Extended Data Fig. 4b and Extended Data Fig. 4c**). Only the R71A mutation significantly
195 enhanced the neutralization activity of 19-77 against the viruses tested, including the
196 restoration of neutralizing activity against JD.1.1 and EG.5-A475V. We therefore introduced

197 the other 18 possible amino-acid substitutions to the R71 position of 19-77 and then evaluated
198 their neutralization efficacy against the same panel of resistant viruses (**Extended Data Fig.**
199 **4d**). Except for R71K, all other substitutions resulted in not only improved neutralization
200 activities against EG.5 and HK.3 relative to the original antibody, but also restoration of
201 activity against JD.1.1 and EG.5-A475V. Overall, the extent of improvement for these mutant
202 antibodies (19-77Δs) ranged from 3- to >100-fold, with aliphatic substitutions R71A, R71L,
203 and R71V being the best (**Fig. 3b and Extended Data Fig. 4d**).
204
205 Structural analysis showed that R71 of 19-77 forms hydrogen bonds with S30 of CDRH1 and
206 P53 of CDRH2, likely contributing to antibody stability (**Fig. 3c**). Additional modeling
207 indicated that mutating R71 could disrupt these hydrogen bonds, with the exception of R71K,
208 which could also form similar interactions (**Fig. 3d**). We then hypothesized that R71 might
209 restrict the motion of CDRH1 and CDRH2 of 19-77, and that mutating this arginine could lead
210 to greater antibody flexibility. To test this hypothesis, we conducted molecular dynamics (MD)
211 simulations for 19-77 with either arginine or alanine at position 71 of the heavy chain. The
212 results showed that A71 increased the range of motion of the heavy-chain CDRs compared to
213 R71 (**Extended Data Movie 1**). Moreover, the fluctuations in the movement of each residue
214 for the A71 variant of 19-77 were noticeably greater than those in the original antibody,
215 especially within the CDRs (**Fig. 3e**). These findings, in turn, suggested that the increased
216 flexibility of the A71 variant could allow the antibody to better accommodate for certain
217 mutations in the SARS-CoV-2 spike.
218
219 We next assessed the *in vitro* neutralizing activity of the R71A, R71L, and R71V versions of
220 19-77 (designated 19-77ΔA, 19-77ΔL, and 19-77ΔV, respectively) against a large pseudovirus
221 panel comprising of 32 SARS-CoV-2 variants and 5 SARS-CoV-2-like sarbecoviruses.
222 Control antibodies included the original 19-77, along with the recently authorized pemivibart
223 (VYD222)[33] and a published broadly neutralizing mAb, P4J15[41] (**Fig. 4**). The engineered 19-
224 77 variants consistently showed better virus neutralizing potency and breadth compared to the
225 parental antibody. Importantly, against viruses that are widely circulating today, the
226 improvements were substantial: 7.7-to-9.2-fold for JN.1, 6.2-to-7.8-fold for KP.2, 8.1-to-13.3-
227 fold for KP.3, 16.2-to-21.6-fold for KP.3.1.1, and >50.0-to-147.1-fold for XEC, with the latter
228 two being most relevant presently. The activity P4J15 was either severely impaired or knocked
229 out by JN.1 and its progeny viruses. Pemivibart showed decreased potency against recent JN.1
230 sublineages, particularly KP.3.1.1 and XEC, and completely lost activity against MC.10.1.
231 These results showed that the optimized 19-77 mAbs possess the requisite antiviral properties
232 to be considered as candidates for clinical development, pending a full developability
233 assessment. Reassuringly, the three mutations at R71 did not adversely impact antibody
234 expression, aggregation propensity, or pharmacokinetics in mice (**Extended Data Fig. 5**).
235
236 **Impact of R71 mutations on other VH3-53/66 class of mAbs to the viral spike**
237
238 Monoclonal 19-77 belonged to the VH3-53/66, multi-donor class of SARS-CoV-2 neutralizing
239 mAbs that target the class 1 region of RBD[39]. We therefore explored whether the same set of

240 R71 mutations could similarly benefit other members of this antibody class. Mutations R71A,
241 R71L, and R71V were then introduced into five VH3-53/66 class mAbs, including BD56-
242 1302[42], BD56-1854[42], Omi-3[43], 19-79, BD57-0129[42], and BD-515[44], as well as two non-VH3-
243 53/66 class mAbs, C68.59[29] and Omi42[43], serving as controls. The original mAbs and their
244 modified antibody variants were then assayed for their neutralizing activity against a panel of
245 pseudoviruses (**Extended Data Fig. 6**). All unmodified mAbs showed partial or complete loss
246 of neutralizing activity against some later Omicron subvariants such as EG.5.1, HK.3, JD.1.1,
247 and JN.1. In contrast, every modified VH3-53/66 mAb exhibited improved neutralization
248 capability, albeit with varying magnitudes (3- to >100-fold), whereas no improvement was
249 observed for non-VH3-53/66 mAbs (**Fig. 5 and Extended Data Fig. 6**). In fact, a number of
250 modified mAbs regained the ability to neutralize subvariants that had been completely resistant
251 to their unmodified counterparts. For example, BD57-0129 failed to neutralize JN.1 or HK.3,
252 but its modified counterparts neutralized both viruses robustly. The extension of the benefit of
253 R71 mutations to mAbs other than 19-77 suggests that the responsible mechanism is not likely
254 to operate solely at the interface with the paratope. Instead, the broader benefit observed is
255 consistent with the hypothesis of greater conformational flexibility of the antibody CDRs
256 discussed previously. Additionally, antibodies using VH3-53 in the human B-cell repertoire
257 very rarely carry a mutation at R71 (**Extended Data Fig. 7**), highlighting the uniqueness of
258 our engineered mAbs compared to those found after SARS-CoV-2 infections.
259
260 **Molecular insights into enhanced virus neutralization by 19-77ΔV**
261
262 To further explore the mechanism of the enhancement of virus neutralization by mutating R71,
263 we determined two additional cryoEM structures: the Fabs of 19-77ΔV and S309 in complex
264 with HK.3 or JD.1.1 RBD at 2.9 Å and 3.1 Å resolution, respectively (**Fig. 6a and Extended**
265 **Data Fig. 3**). We then compared these structures by aligning their RBDs with that of the 19-
266 77-D614G complex and measuring the alpha carbon (Cα) distances for each heavy chain
267 residue in 19-77 against the D614G complex. The analysis showed that the Cα distances in
268 19-77ΔV, when bound to HK.3 and JD.1.1 RBDs, were significantly greater (0.99 Å and 0.91
269 Å, respectively) compared to the original 19-77 in complex with HK.3 RBD (0.76 Å) (**Fig. 6b**).
270 Moreover, the motion of the CDRH1 and CDRH2 were observed directly across these
271 structures, and the valine substitution at residue 71 resulted in the loss the hydrogen bonds that
272 had existed between R71 and the residues S30 and P53 in the heavy chain (**Fig. 6c**). In addition,
273 the CDRH3 in 19-77ΔV exhibited a shift of 1 Å compared to the original 19-77, resulting in
274 an increased distance (from 3.3 Å to 3.6 Å) between residues P100 and F455 (**Fig. 6d**). This
275 change mitigated the slight van der Waals clash between these two residues in HK.3 RBD and
276 19-77 complex (**Fig. 2e**). Lastly, the distance between V475 in the JD.1.1 RBD and N32 of
277 the heavy chain of 19-77ΔV increased to 3.2 Å from the 2.0 Å found in the original 19-77
278 bound to D614G RBD (**Fig. 6e**), showing the mitigation of steric hindrance caused by the
279 A475V mutation. Collectively, these findings support the notion that 19-77Δ mAbs are indeed
280 more flexible and therefore more accommodating for the mutations found in emerging SARS-
281 CoV-2 variants.
282

283 ***In vitro* selection of SARS-CoV-2 resistant to 19-77ΔV**
284
285 Although the SARS-CoV-2-neutralization breadth and potency of the optimized 19-77 variants
286 were impressive (**Fig. 4**), our expectation was that the virus will still find a way to escape given
287 its history of evading all COVID-19 mAbs authorized to date. We therefore undertook two
288 sets of *in vitro* studies to define its mutational pathways to resist 19-77ΔV. First, we performed
289 serial passaging of the authentic JN.1 virus in increasing antibody concentrations (0.1 to 50
290 μg/mL) in Vero-ACE2-TMPRSS2 cell over 15 days (under 3 days per passage). After five
291 passages, a resistant virus was sequenced and found to carry mutations F456S (TTT to TCT)
292 and K554E (AAG to GAG, **Fig. 7a**). When these mutations were introduced into the JN.1
293 pseudovirus, the resultant pseudovirus showed a 33-fold greater resistance to 19-77ΔV, and
294 even more to 19-77. Additional studies showed that the antibody evasion was attributable
295 solely to F456S, while K554E partially compensated for the loss in viral fitness (**Extended**
296 **Data Fig. 8a and Extended Data Fig. 8b**). Notably, this combination of mutations is
297 extremely rare (0.0002%) in the GISAID database.
298
299 Second, we also utilized a replication-competent VSV bearing the JN.1 spike to select for
300 variants that could escape from 19-77ΔV. This selection was performed in 66 replicates in 24-
301 well plates, involving four rounds of selection over 8 days in Vero-E6-TMPRSS2-T2A-ACEs
302 cells with increasing concentrations of 19-77ΔV (0.4 to 50 μg/mL). At the end of this process,
303 escape variants were detected in 11 wells, and sequencing of their spike genes revealed 8
304 distinct single or double mutations (**Fig. 7b**). Notably, all these mutations resulted from single
305 nucleotide changes but were rarely found in the GISAID database, with frequencies ranging
306 from 0% to 0.01%, and each of the pseudoviruses constructed with these mutations exhibited
307 impaired infectivity compared to the JN.1 pseudovirus, ranging from 1% to 33% (**Fig. 7b and**
308 **Extended Data Fig. 8c**). Furthermore, these pseudoviruses demonstrated increased resistance
309 to soluble hACE2 inhibition (**Fig. 7b and Extended Data Fig. 8d**), indicating a loss in receptor
310 affinity, perhaps accounting in part for their reduced infectivity. Single mutations G485D
311 (GGC to GAC) and Y489H (TAC to CAC), both residing in the RBD, decreased the
312 neutralization activity of 19-77ΔA/L/V considerably (9- to 121-fold), whereas the remaining
313 mutations completely abolished the neutralization activity of the three optimized mAbs (**Fig.**
314 **8b and Extended Data Fig. 8d**).
315
316 *In silico* structural analysis showed that each of the escape viruses contained a mutation within
317 the epitope of 19-77ΔV that impaired antibody binding (**Fig. 7c**). A475D, G476D, and N487H
318 caused steric hindrance to antibody binding, F465S mutation and residue S455 in JN.1
319 significantly reduced hydrophobic interactions between the antibody and RBD. Furthermore,
320 both Y473S and Y489H abolished hydrogen bonds with the antibody, contributing to the
321 dramatic drop in neutralization observed for the escape viruses with these mutations.

Discussion

In this study, we present findings on the characterization of a human IGHV3-53-derived monoclonal antibody, 19-77, which exhibited neutralizing activity against most but not all SARS-CoV-2 variants (**Fig. 1b and Fig. 4**). Strikingly, 19-77 featured the shortest CDRH3 (9 amino acids) while containing the highest degree of somatic hypermutations among its class of mAbs (**Fig. 1c**). Structural analysis revealed that 19-77 recognized the spike RBD in the "up" position (**Fig. 1d**), and its epitope overlapped with the ACE2 footprint (**Fig. 2a**). Subsequent *in silico* energy calculations (**Extended Data Fig. 4a)** and empirical mutagenesis experiments (**Fig. 3a and Fig. 4b**) yielded modified antibodies 19-77ΔA, 19-77ΔL, and 19-77ΔV, each of which neutralized all 32 SARS-CoV-2 variants tested, including KP.3.1.1 and XEC that are so prevalent today (**Fig. 4**). These optimized antibodies joined a limited list of human mAbs that possess sufficiently potent neutralizing activity against all viral variants, such as SA55[45], BD55-1205[46], and VIR-7229[47] that target an epitope overlapping with that of 19-77, as well as CYFN1006-1[48] that targets a RBD class 3 epitope. However, we showed that SARS-CoV-2 could easily escape from neutralization by 19-77ΔV *in vitro* (**Fig. 7**). In fact, the virus found multiple solutions to evade our optimized antibody, albeit with a fitness cost. Such an outcome was, more or less, expected given how SARS-CoV-2 has evolved in the population to render inactive all clinical mAbs authorized prior to 2024. Indeed, pemivibart (VYD222) that was authorized only months ago for use as prophylaxis against COVID-19 in immune deficient subjects is already seriously threatened by the emergence of KP.3.1.1 and XEC subvariants[35, 49, 50].

It has been a daunting challenge, as well as a frustrating endeavor, to develop therapeutic or prophylactic mAbs to keep up with the rapid pace of SARS-CoV-2 evolution. Yet the reality is that millions of individuals worldwide are sufficiently immunocompromised that they cannot benefit from the protection conferred by COVID-19 vaccines. Such persons need effective prophylaxis with passively administered virus-neutralizing mAbs, as was conferred previously by the combination of tixagevimab and cilgavimab known as Evusheld[51] and presently by pemivibart[52]. Going forward, we believe one of our optimized 19-77Δ mAbs would qualify as a compelling candidate for clinical development given its superior potency and breadth against all SARS-CoV-2 variants known to date (**Fig. 4**), as well as its lack of discernible developability challenges to date (**Extended Data Fig. 5**). The potential clinical utility of an optimized 19-77Δ could be further improved if used in combination with a non-competing, broadly neutralizing mAb like CYFN1006-1[48]. Additionally, the use of antibody cocktails may help reduce the likelihood of generating escape variants during antiviral mAb therapy[53, 54].

Herein, we also present a unique strategy for optimizing the activity of a monoclonal antibody by increasing its conformational flexibility. Traditionally, antibody engineering had been focused primarily on increasing the binding affinity using a number of approaches, including chain shuffling[55, 56], site-directed mutagenesis[57], phage and other display technologies[58-62], and structure-based or artificial-intelligence-guided methods[63-65]. Such methodologies, typically, had been designed to increase antibody affinity by modifying the CDR residues at the antibody-antigen interface. Other antibody approaches to optimize antibody activity included the use of

366 multivalency with the creation of "multabodies"[66], or the strategic addition of a glycan to bulk
367 up a steric hindrance effect[67]. The framework regions of a mAb were seldom touched, because
368 they are crucial for maintaining the proper orientation and conformation of the CDRs[68, 69]. In
369 our study on 19-77, however, *in silico* energy calculations indicated that a single amino-acid
370 substitution at residue 71 in framework region 3 of the heavy chain could improve antibody
371 binding to the viral spike (**Extended Data Fig. 4a**), which was proven correct experimentally
372 by replacing the arginine with any other natural amino acid except for lysine (**Fig. 3a, Fig. 3b,**
373 **and Fig. 4**). The improved activity of optimized 19-77Δ mAbs was attributable to the loss of
374 hydrogen bonding by R71 (**Fig. 3c and Fig. 6c**), leading to greater flexibility of the CDRs as
375 shown by molecular dynamics (**Fig. 3e**) and structural analyses (**Fig. 6**). This enhanced
376 conformation flexibility, in turn, allowed each optimized antibody to be more tolerant of
377 mutations within or near its epitope, ultimately resulting in the striking SARS-CoV-2
378 neutralization potency and breadth observed (**Fig. 4**). Remarkably, this optimization strategy
379 was also successfully applied to 6 other IGHV3-53/3-66-derived human mAbs that target the
380 same epitope cluster as 19-77 (**Fig. 5**). But its applicability did not extend to other SARS-
381 CoV-2-neutralizing mAbs that utilize other VH germline genes, suggesting a specific mutation
382 at framework residue 71 is not likely to confer a generalizable benefit to other mAbs.
383 Nevertheless, the general concept of modifying antibody conformational flexibility should be
384 further explored in other settings by other means. Increasing conformational rigidity could
385 lead to improved antibody-antigen affinity, as has been reported for an IGHV4-59-encoded
386 anti-lysozyme mAb[70]. On the other hand, increasing conformational flexibility, as shown in
387 this study, could allow the antibody to better tolerate sequence variations in the target antigen.
388 Such an approach may be useful for monoclonal antibodies directed to polymorphic antigens
389 or surface proteins of rapidly evolving viruses such as HIV-1, coronaviruses, influenza viruses,
390 and hepatitis C virus. It may be another important conceptual tool in our antibody engineering
391 armamentarium.

Figures and legends

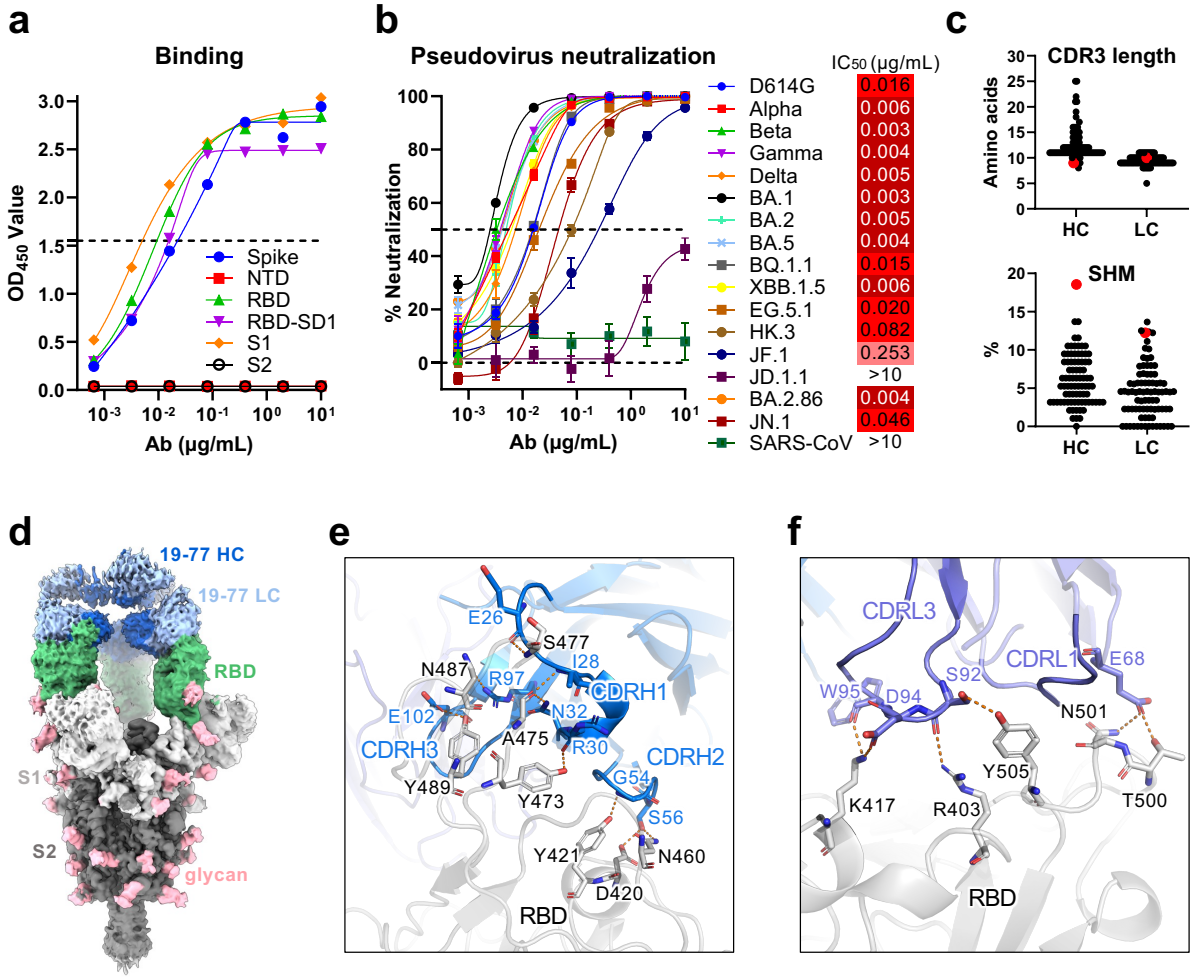

Fig. 1 | Neutralization activity and epitope mapping of 19-77.

a. Binding of 19-77 to the indicated antigens of SARS-CoV-2 D614G tested by ELISA.

b. Neutralization IC_{50} values of 19-77 against pseudotyped SARS-CoV-2 variants and SARS-CoV, with the IC_{50} of each virus is denoted. Neutralization curves are shown as mean ± standard error of mean (SEM) from technical triplicates.

c. Complementarity-determining region 3 (CDR3) lengths and somatic hypermutations (SHM) of 19-77 heavy chain (HC) and light chain (LC), compared with other 3-53 and 3-66 antibodies. 19-77 is highlighted in red.

d. Cryo-EM reconstruction of 19-77 in complex with the SARS-CoV-2 D164G spike protein, at a resolution of 2.45Å.

e. Key interactions between 19-77 heavy chain and the D614G RBD. Hydrogen bonds are shown as the orange dashed lines.

f. Key interactions between 19-77 light chain and the D614G RBD. Orange dashed lines indicate hydrogen bonds.

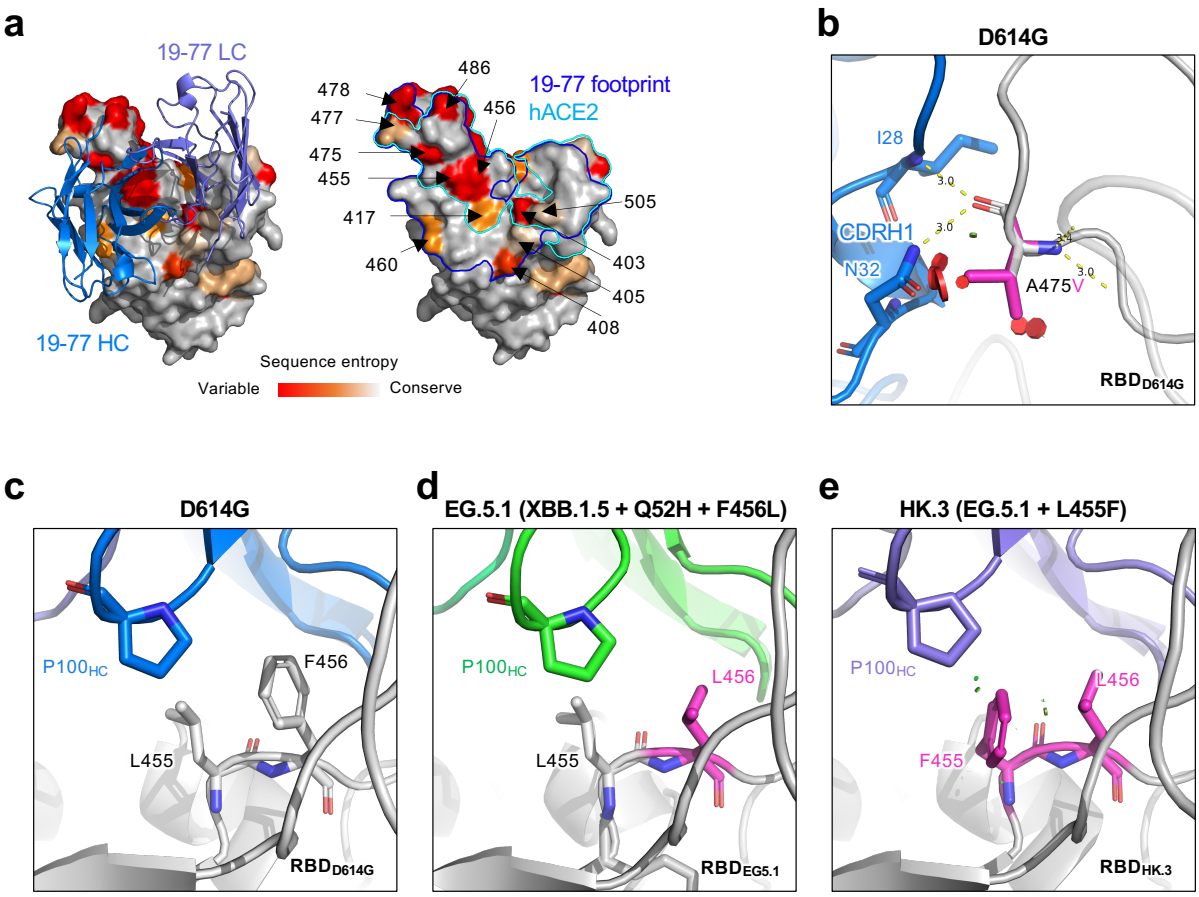

Fig. 2 | Sequence conservation and resistant mutations in the 19-77 epitope.

a. Top view of the RBD inner face in complex with the 19-77 antibody. 19-77 heavy chain and light chain are shown in marine and light blue, respectively. The residues in the RBD are colored by the sequence entropy in circulating SARS-CoV-2 variants. The blue and cyan boundaries show the footprints of 19-77 and human ACE2 (hACE2), respectively.

b. Structure modeling of how A475V on the RBD affects 19-77 neutralization. The clashes are shown as red plates.

c-e. Comparison of residues 455 and 456 on RBD and P100$_{HC}$ in D614G (**c**), EG.5.1 (**d**) and HK.3 (**e**) structures. The van der Waals clashes are shown as green plates.

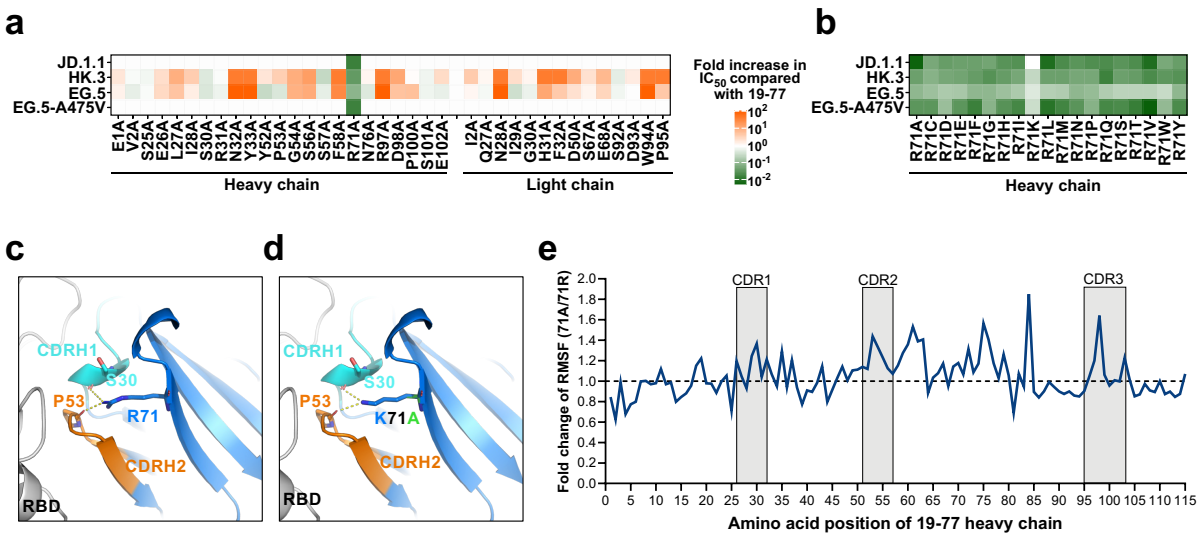

Fig. 3 | Optimization of 19-77 in neutralization activity.

a. Neutralization of 19-77 carrying individual mutations on both heavy and light chains, in comparison with the wildtype 19-77 antibody.

b. Neutralization of 19-77 carrying various amino acid substitutions at R71 on the heavy chain, compared with the wildtype 19-77 antibody.

c. Depiction of the interactions between R71 and the heavy chain CDRs H1 (cyan) and H2 (orange) in 19-77. Dashed lines indicate the presence of hydrogen bonds.

d. Structure modeling of K71 (blue) and A71 (green) with HCDRs of 19-77. Dashed lines indicate the presence of hydrogen bonds between 19-77ΔK.

e. Comparison of the RMSF between the Fab regions of 19-77 and its mutant 19-77ΔA. The Y-axis represents the fold change in RMSF per residue in 19-77ΔA relative to 19-77. The X-axis displays the positional numbering of residues within the antibody. RMSF, per-residue root-mean-square fluctuation.

Clade	Pseudovirus	19-77	19-77 mutants			Control Abs	
			R71A	R71L	R71V	P4J15	VYD222
SARS-CoV-2 variants	D614G	0.015	0.009	0.007	0.009	0.004	0.013
	B.1.1.7 (Alpha)	0.003	0.003	0.003	0.003	0.003	0.012
	B.1.351 (Beta)	0.003	0.003	0.002	0.002	0.003	0.017
	P.1 (Gamma)	0.002	0.002	0.002	0.002	0.003	0.028
	B.1.617.2 (Delta)	0.005	0.004	0.004	0.004	0.003	0.011
	BA.1	0.001	0.001	0.001	0.001	0.001	0.203
	BA.2	0.008	0.004	0.004	0.004	0.003	0.102
	BA.5	0.006	0.004	0.004	0.004	0.010	0.101
	BA.2.75	0.015	0.007	0.007	0.009	0.004	0.516
	CH.1.1	0.010	0.006	0.009	0.009	0.026	0.381
	DV.7.1	0.285	0.019	0.031	0.025	1.179	1.250
	XBC.1.6	0.007	0.003	0.005	0.004	0.033	0.183
	BQ.1.1	0.011	0.008	0.006	0.009	0.023	0.260
	XBB.1.5	0.008	0.005	0.004	0.008	0.059	0.215
	XBB.1.16.6	0.054	0.004	0.002	0.003	0.017	0.243
	XBB.2.3	0.012	0.007	0.008	0.009	0.018	0.263
	EG.5.1	0.020	0.008	0.006	0.008	0.039	0.233
	FL.1.5.1	0.056	0.006	0.006	0.008	0.039	0.240
	JF.1	0.156	0.008	0.006	0.008	0.227	0.343
	HV.1	0.052	0.006	0.005	0.006	0.020	0.159
	HK.3	0.107	0.007	0.006	0.008	1.340	0.304
	JD.1.1	>10	0.033	0.032	0.058	0.355	0.288
	BA.2.87.1	0.026	0.008	0.009	0.009	0.003	1.043
	BA.2.86	0.006	0.003	0.003	0.003	0.081	0.459
	JN.1	0.046	0.005	0.005	0.006	>10	0.070
	JN.4	0.017	0.004	0.003	0.003	0.270	0.512
	LB.1	0.087	0.008	0.009	0.008	2.303	0.208
	KP.2	0.031	0.004	0.005	0.004	>10	0.148
	KP.3	0.585	0.044	0.072	0.068	0.729	0.554
	KP.2.3	0.107	0.015	0.009	0.005	>10	0.459
	KP.3.1.1	1.426	0.066	0.088	0.075	2.862	1.217
	XEC	>10	0.092	0.200	0.068	>10	1.998
	LP.8.1	>10	0.105	0.175	0.072	>10	0.939
	LP.8.1.1	>10	0.095	0.114	0.058	>10	0.845
	MC.10.1	>10	0.324	0.278	0.083	>10	>10
	LF.7	0.26	0.02	0.017	0.012	>10	0.405
SARS-CoV-2 like sarbecoviruses	GX-pangolin	1.878	0.302	0.317	0.163	>10	0.008
	RaTG13	0.005	0.003	0.002	0.003	0.004	>10
	BANAL52	0.027	0.015	0.007	0.011	0.007	0.008
	BANAL236	0.012	0.007	0.005	0.011	0.003	0.005
	GD-pangolin	0.009	0.006	0.004	0.006	0.003	0.003

IC_{50} (μg/mL) <0.01 | 0.01-0.1 | 0.1-1 | 1-10 | >10

Fig. 4 | Neutralization activity of 19-77 and 19-77ΔA/L/V against the indicated pseudoviruses. Neutralization IC_{50} values of the indicated antibodies against a panel of pseudotyped viruses, including SARS-CoV-2 variants and SARS-CoV-2-like sarbecoviruses.

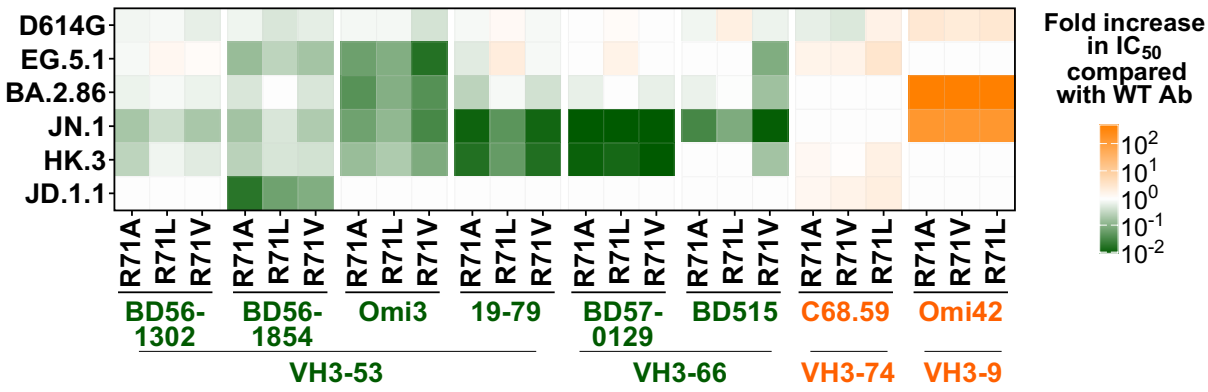

Fig. 5 | R71A/L/V sensitize the neutralization activity of other VH3-53/66 class antibodies. Neutralization of the indicated antibodies from VH3-53/66 and other classes carrying R71A/L/V mutations, compared with the respective wildtype (WT) antibodies.

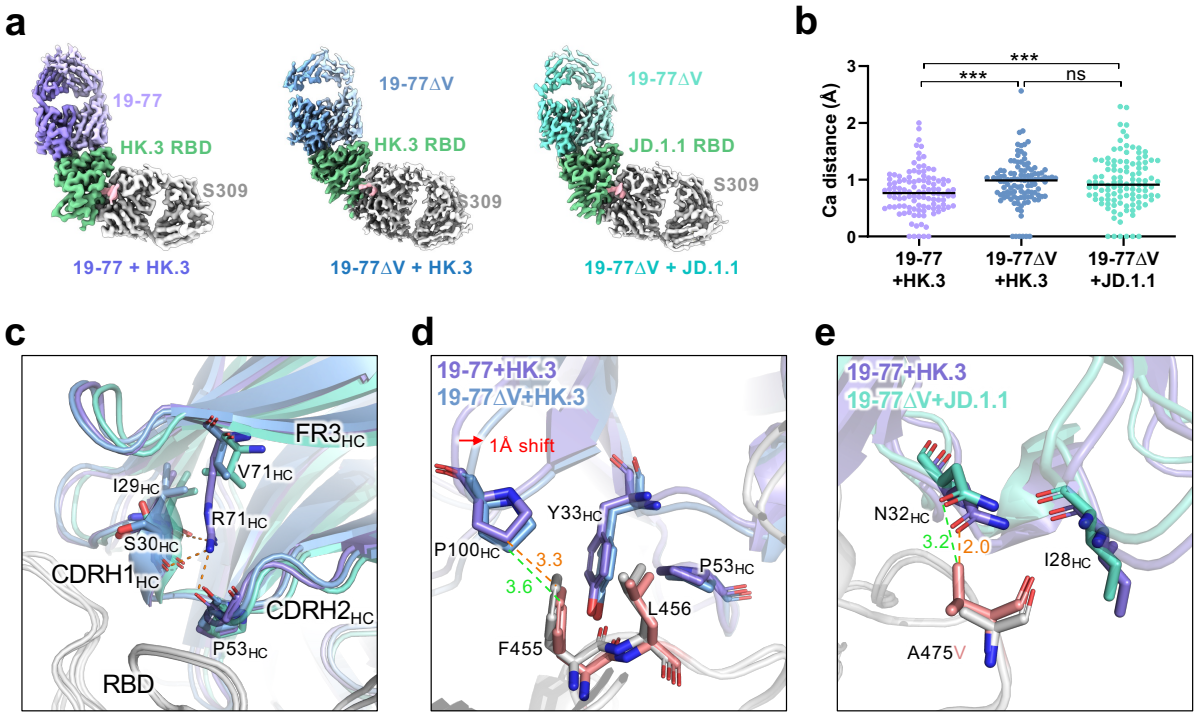

Fig. 6 | Molecular basis of 19-77ΔV accommodating mutations in HK.3 and JD.1.1.

a. Cryo-EM maps of 19-77 and 19-77ΔV Fabs bound to SARS-CoV-2 RBD variants.

b. Distribution of Cα distance for the heavy chain residues of 19-77 in **A** compared with 19-77 in the D614G complex. The structures are aligned based on RBD. Comparisons were made by student's *t*-tests. ***, $p < 0.001$. ns, not significant.

c. Comparison of CDRH1, CDRH2, and R71V in the alignments of 19-77 structures. The hydrogen bonds are shown as orange dashed lines.

d. Interaction details of $P100_{HC}$ in 19-77 and 19-77ΔV with F455 and L456 in the HK.3 RBD. The orange and green dashed lines represent the distances between $P100_{HC}$ and F455 in 19-77 and 19-77ΔV, respectively.

e. Interaction details of $N32_{HC}$ in 19-77 and 19-77ΔV with A475V in the D614G and JD.1.1 RBDs. The orange and green dashed lines represent the distances between V475 and N32 in 19-77 and 19-77ΔV, respectively.

a

mAb	Authentic virus for escape selection	Selection passages	Escape mutations	Frequency of mutations in GISAID	Relative infectivity of pseudotyped escape variant	Fold change in IC_{50} of pseudotyped escape variants compared with the relative WT virus		
						19-77	19-77ΔV	hACE2
19-77ΔV	JN.1	P5	F456S+K554E	0.0002%	64%	<-99	-33	-2.2

b

Escape mutations under sequentially increased 19-77ΔV concentrations				Properties of escape variants from 50 μg/ml of 19-77ΔV selection					
				Frequency in GISAID	Relative infectivity	Fold change in IC_{50} compared with JN.1			
No.	4 μg/ml	20 μg/ml	50 μg/ml			19-77ΔA	19-77ΔL	19-77ΔV	hACE2
1	T393A	T393A/Y489H	T393A/Y489H	0%	1%	<-1214	<-1097	<-1236	<-114
2	F456S	F456S	F456S/E471G	0%	2%	<-1214	<-1097	<-1236	-103
3	Y473S	Y473S	Y473S	0.00036%	1%	<-1214	<-1097	<-1236	<-114
4	A475D	A475D	A475D	0.0035%	2%	<-1214	<-1097	<-1236	<-114
5	G476D	G476D	G476D/N487H	0%	1%	<-1214	<-1097	<-1236	<-114
6	G485D	G485D	G485D	0.010%	33%	-9.0	-12	-10	-12
7	Y489H	Y489H	Y489H	0.0028%	18%	-44	-57	-121	-27
8	Y489H	Y489H	N405D/Y489H	0%	22%	<-1214	<-1097	<-1236	-34

Resistant	<-1000	<-100	<-10	<-3

c

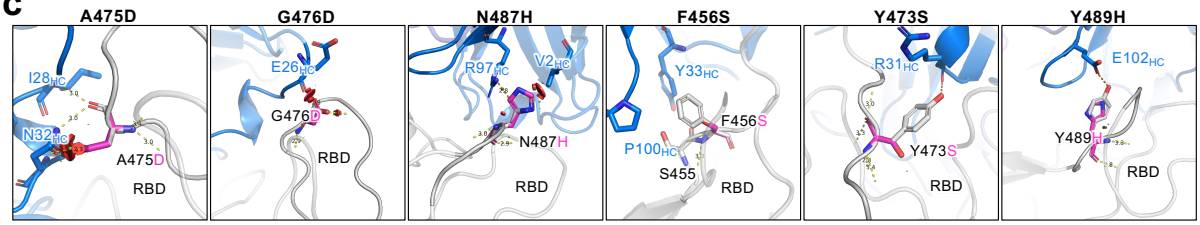

Fig. 7 | *In vitro* selection of 19-77 resistant mutations.

a. Properties of the authentic JN.1 escape variant selected under the pressure of 19-77ΔV.

b. Properties of the replication-competent VSV-JN.1 escape variants selected under the pressure of 19-77ΔV.

c. Structural modeling of how A475D, G476D, N487H, F456S, Y473S, and Y489H affect 19-77 neutralization. The clashes are shown as red plates, and the hydrogen bonds are shown as orange dashed lines.

464 **Methods**
465
466 **Human subject**
467 Blood sample from Donor 19, a 41-year-old Asian male, was collected at Columbia University
468 Irving Medical Center. Donor 19 was confirmed for a BA.5 infection by PCR sequencing
469 (Single Nucleotide Polymorphisms) and provided written informed consent. Sample
470 collections were performed under protocols reviewed and approved by the Institutional Review
471 Board of Columbia University. Clinical information of Donor 19 is provided in **Extended Fig.**
472 **1a**.
473
474 **Cell lines**
475 Vero-E6 (CRL-1586) and HEK293T (CRL-3216) cells were purchased from the American
476 Type Culture Collection (ATCC). Expi293 cells (A14527) were purchased from Thermo
477 Fisher Scientific. Vero-E6-TMPRSS2-T2A-ACE2 (NR-54970) were obtained from BEI
478 Resources. 293T-ACE2 were kindly provided by Dr. Jesse D. Bloom. Morphology of each
479 cell line was confirmed visually before use. All cell lines tested mycoplasma negative. Vero-
480 E6 and Vero-E6-TMPRSS2-T2A-ACE2 cell lines are from African green monkey kidneys.
481 HEK293T, 293T-ACE2, and Expi293 cells are of female origin.
482
483 **Plasmid construction**
484 SARS-CoV-2 spike-expressing plasmids for D614G, Alpha, Beta, Gamma, Delta and Omicron
485 were previously generated[13, 20, 21, 27]. Expressing constructs for the spike proteins of SARS-
486 CoV-2-like sarbecoviruses were either previously generated[71] or newly generated by
487 synthesizing (GenScript) spike genes and then cloned into the pCMV3 vector. To generate the
488 expression constructs for soluble spike trimer (S2P) proteins, the ectodomains (1-1208aa,
489 numbering based on WA1) of the spikes were PCR amplified and cloned into the paH vector
490 and then introduced K986P and V987P substitutions, as well as a "GSAS" substitution of the
491 furin cleavage site (682-685aa in WA1) into the spikes[72]. SARS-CoV S2P was fused with an
492 AVI tag at the C terminus and D614G and XBB.1.5 S2P spikes were tagged with a 6×His tail
493 also at the C terminus. To make SARS-CoV-2 RBD-expressing construct, RBD region (319-
494 537aa) of each variant was fused with a 6×His tag and then cloned into the p3BNC vector. All
495 constructs were confirmed by Sanger sequencing.
496
497 Antibody expressing constructs were generated as previously described[38]. The variable regions
498 of heavy and light chains for each antibody were synthesized (GenScript) and then cloned into
499 the gWiz vector. To make spike/antibody plasmid constructs carrying individual mutations,
500 the Q5® Site-Directed Mutagenesis Kit (NEB) was utilized following the manufacturer's
501 instructions.
502
503 **Protein purification**
504 To make human ACE2-Fc (hACE2) protein, pcDNA3-sACE2-WT(732)-IgG1[73] (Addgene
505 plasmid #154104, gift of Erik Procko) plasmid was transfected into Expi293 cells using 1
506 mg/mL polyethyleneimine (PEI) at a ratio of 1:3, and the supernatants were collected after five
507 days. hACE2 was purified from the cell supernatant by using rProtein A Sepharose (GE). For

508 antibody purification, both heavy and light chains of each antibody were transfected at a ratio
509 of 1:1 into Expi293 cells using PEI. And the expressed antibody in the cell supernatant was
510 purified using the same method as for hACE2 purification. For the spike trimer proteins or
511 RBD proteins, paH-spike or p3BNC-RBD, respectively, was transfected into Expi293 cells
512 using PEI at a ratio of 1:3, and the supernatants were collected five days later. The His tagged
513 and the AVI tagged proteins were purified using Excel resin (Cytiva) and Agarose bound
514 Galanthus nivalis lectin (VectorLabs, AL-1243-5) according to the manufacturers' instructions.
515 The molecular weight and purity were checked by running the proteins on SDS-PAGE.
516
517 After purification of 19-77 and 19-77ΔA/L/V, 100 µg of each antibody was prepared and run
518 through a Superdex 200 Increase 10/300 GL column to generate their size exclusion
519 chromatography (SEC) profiles. AVI tagged SARS-CoV S2P protein were biotinylated using
520 the BirA biotin-protein ligase standard reaction kit (Avidity LLC; BirA500) following the
521 manufacturer's instructions.
522
523 **ELISA**
524 50 ng per well of an antigen such as S2P spike, NTD (ACROBiosystems, S1D-C52H6), RBD
525 (ACROBiosystems, SPD-C52H1), RBD-SD1 (Exonbio, 19Cov-S130), S1 (ACROBiosystems,
526 S1N-C52H3), or S2 (ACROBiosystems, S2N-C52H2) was coated onto ELISA plates at 4°C
527 overnight. The ELISA plates were then blocked with 300 µL of blocking buffer consisting of
528 phosphate-buffered saline (PBS) with 1% bovine serum albumin and 20% bovine calf serum
529 (Sigma-Aldrich) at 37°C for 2 hours. Afterwards, 100 µL of 5-fold serially diluted antibodies
530 was added and then incubated at 37°C for 1 hour. Next, 100 µL of 10,000-fold diluted
531 Peroxidase AffiniPure goat anti-human IgG Fcγ fragment-specific antibody (Jackson
532 ImmunoResearch, catalog no. 109-035-170, RRID: AB_2810887) was added into each well
533 and incubated for another 1 hour at 37°C. The plates were washed between each step with
534 PBST (0.5% Tween-20 in PBS). Last, 3,3′,5,5′-tetramethylbenzidine (TMB) substrate (Sigma-
535 Aldrich) was added and incubated before the reaction was stopped using 1 M sulfuric acid.
536 Absorbance was measured at 450 nm.
537
538 **Antibody pharmacokinetics in mice**
539 All animal experiments were carried out in strict accordance with the Policy on Humane Care
540 and Use of Laboratory Animals of the United States Public Health Service. The protocol was
541 approved by the Institutional Animal Care and Use Committee (IACUC) at The Columbia
542 University (Animal Welfare Assurance no. D16-00003). Retrobulbular blood collections for
543 antibody pharmacokinetics were conducted using approved anesthesia and/analgesics under
544 the protocol. Mice were euthanized with CO2, with every effort made to minimize suffering
545 following the guidelines. 100 µg (1 mg/mL) of each antibody was intraperitoneally (ip) injected
546 into Balb/c mice (3 mice for each antibody). Mouse blood was collected on day 2, 4, 7 and 10
547 post ip injection and antibody concentrations in serum were measured by ELISA. Briefly, 100
548 ng goat anti-human IgG Fc antibody (Cat: 109-005-008, JacksonImmunoResearch) was coated
549 per well in 96-well plates overnight and the ELISA plates were then blocked with 300 µL of
550 blocking buffer consisting of PBS with 1% bovine serum albumin and 20% bovine calf serum
551 (Sigma-Aldrich) at 37°C for 2 hours. Afterwards, 100 µL of 3-fold serially diluted serum or

552 2-fold serially diluted purified antibody was added and then incubated at 37°C for 1 hour. Next,
553 100 μL of 10,000-fold diluted Peroxidase AffiniPure goat anti-human IgG H+L HRP (Cat:
554 109-035-088, JacksonImmunoResearch) was added into each well and incubated for another 1
555 hour at 37°C. The plates were washed between each step with PBST (0.5% Tween-20 in PBS).
556 Last, TMB substrate (Sigma-Aldrich) was added and incubated before the reaction was stopped
557 using 1 M sulfuric acid. Absorbance was measured at 450 nm.
558
559 **Pseudovirus production and infectivity**
560 SARS-CoV-2 pseudoviruses were generated as previously described[38]. In brief, HEK293T
561 cells were transfected with a spike-expressing construct using 1 mg/mL PEI and then infected
562 with VSV-G pseudotyped ΔG-luciferase (G*ΔG-luciferase, Kerafast) one day post-
563 transfection. Two hours after infection, cells were washed three times with PBS, changed to
564 fresh medium, and then cultured for one more day before the cell supernatants were harvested.
565 Pseudoviruses in the cell supernatants were clarified by centrifugation, aliquoted, and stored at
566 -80°C.
567
568 To evaluate the infectivity of the pseudotyped escape variants of 19-77 and 19-77ΔV, fresh
569 pseudoviruses without freezing and thawing were serially titrated from 50 μL with a dilution
570 factor of 3 and then inoculated into Vero-E6 cells. After overnight culture, Vero-E6 cells were
571 harvested and quantified for luciferase activity using the Luciferase Assay System (Promega).
572
573 **Pseudovirus neutralization assay**
574 To normalize the viral input between assays before conducting the neutralization assays,
575 pseudoviruses of SARS-CoV and SARS-CoV-2 variants and SARS-CoV-2-like
576 sarbecoviruses were titrated on Vero-E6 cells and 293T-ACE2 cells. Heat-inactivated serum
577 from Donor 19 was serially diluted starting from 1:25 with a dilution factor of four.
578 Monoclonal antibodies were 5-fold serially diluted starting from 20 μg/mL in 96 well plates in
579 triplicate. Then, 50 μL of diluted pseudovirus was added and incubated with 50 μL serial
580 dilutions of serum or mAb for 1 hour at 37°C. During the co-culture, target cells were
581 trypsinized, resuspended with fresh medium, and then added into virus-sample mixture at a
582 density of 4-10 × 10^4 cells/well. The plates were incubated at 37°C for ~12 hours before
583 luciferase activity was quantified using the Luciferase Assay System (Promega) using SoftMax
584 Pro v.7.0.2 (Molecular Devices). Neutralization ID_{50} values for sera and IC_{50} values for
585 antibodies were calculated by fitting a nonlinear five-parameter dose-response curve to the data
586 in GraphPad Prism v.10.
587
588 **Selection of escape mutations.**
589 SARS-CoV-2 isolate Omicron JN.1 (BEI NR-59693) was mixed with serial five-fold dilutions
590 of 19-77ΔV antibody at MOI of 0.2 and incubated for 1 h. Following incubation, the mix was
591 overlaid on a 24-well plate bearing a monolayer of Vero-ACE2-TMPRSS2 cells (BEI NR-
592 54970) to a final volume of 1 mL. Plates were incubated at 37°C/ 5% CO_2 for 70 h till
593 cytopathic effect (CPE) was complete (100%) in virus control wells bearing no antibody. At
594 this time, all wells with antibody dilutions were scored to determine the 50% inhibition titer
595 (EC_{50}) and supernatant collected from this well was used for subsequent round of selection.

596 Passaging of the progeny over new Vero-ACE2-TMPRSS2 cells continued till each of the virus
597 variant was able to form CPE in the presence of 50 μg/mL of the antibody. The resulting
598 supernatant was then collected, and RNA was extracted using QiaAMP Viral RNA kit (Qiagen
599 57704). cDNA was obtained using Superscript IV enzyme (Thermo Scientific 18090010).
600 Spike gene from the cDNA was amplified using limiting dilution nested PCR and sequenced
601 using Sanger sequencing (Genewiz). Multiple clones from limiting dilution nested PCR were
602 sequenced to confirm the dominant mutants in the pool of the resulting progeny viruses and a
603 percentage of their prevalence was calculated from the total number sequenced. At least 8
604 clones were sequenced from each of the passages reported in **Fig. 7**.
605
606 To generate recombinant replication-competent VSV-ΔG bearing the JN.1 spike protein (VSV-
607 ΔG-JN.1), the pVSVΔG-SARS-CoV-2-S_nLucP plasmid was purchased from Kerafast (Cat#
608 EGA292) and its encoding SARS-CoV-2-S gene was replaced with JN.1 spike gene to create
609 pVSVΔG-JN.1_nLucP. The pVSVΔG-JN.1_nLucP plasmid and a set of helper plasmids,
610 including VSV-N, VSV-P, VSV-L, and VSV-G (Kerafast, Cat# EH1012), were then
611 transfected into 293T cells at a ratio of 5:3:5:1:8 using 1 mg/mL PEI-MAX. Before
612 transfection, 293T cells were rinsed with serum-free DMEM, incubated with Vaccinia vTF7-3
613 (Imanis Life Sciences, Cat# REA006) at a MOI of 5 for 45 minutes, and then replaced with
614 fresh medium. Two days post-transfection, the supernatant was harvested and filtered through
615 a 0.22 μm filter to remove cell debris and Vaccinia vTF7-3. The rVSV-ΔG-JN.1 generated
616 from 293T cells was then serially diluted with a dilution factor of 5 and inoculated into Vero-
617 E6-TMPRSS2-T2A-ACE2 cells in 24-well plates for 1 hour. The virus was then washed away,
618 and the cells were cultured at 37°C/5% CO_2 for 16-24 hours. Vero-E6-TMPRSS2-T2A-ACE2
619 cells were monitored, and the virus was harvested from wells in which only one plaque was
620 observed, then filtered and stored at -80°C. The rVSV-ΔG-JN.1 generated from Vero-E6-
621 TMPRSS2-T2A-ACE2 cells was titrated on Vero-E6-TMPRSS2-T2A-ACE2 cells before use.
622 To select escape viruses, rVSVΔG-JN.1 was incubated with 0.4 μg/mL of 19-77ΔV for 1 hour
623 before being added to Vero-E6-TMPRSS2-T2A-ACE2 cells in 24-well plates at a MOI of 0.01.
624 A total of 66 replicates were set up. Two days after coculture, cell supernatants from wells
625 with CPE were harvested, and 100 μL of each supernatant was incubated with 4 μg/mL of 19-
626 77ΔV for 1 hour before another round of infection in pre-seeded Vero-E6-TMPRSS2-T2A-
627 ACE2 cells in 24-well plates. Two days later, supernatants containing escape viruses were
628 further harvested and selected the same way using 20 μg/mL, and then 50 μg/mL, of 19-77ΔV
629 in a stepwise manner. mRNAs of the escape viruses in the supernatants were then extracted
630 using the viral RNA/DNA purification kit (MACHEREY-NAGEL, Cat# 740643) and reverse-
631 transcribed to cDNA using the SuperScript™ VILO™ cDNA Synthesis Kit (Invitrogen, Cat#
632 11754). The RBD genes of the escape viruses were then amplified using primers 5'-
633 GGGCATCTACCAGACCAGCAACTTCA-3' and 5'-
634 GAACACATTGCTGCCTGTGCTGT-3' and sequenced.
635
636 **Antigen-specific memory B cell sorting and single-cell B cell receptor sequencing**
637 Peripheral blood mononuclear cells from Donor 19, and two healthy donors were stained with
638 the LIVE/DEAD Fixable Yellow Dead Cell Stain Kit (Invitrogen) at ambient temperature for
639 20 min, followed by washing with RPMI 1640 complete medium [RPMI 1640 + 10% fetal

640 bovine serum (FBS) + penicillin/streptomycin (P/S) (100 U/mL)] and incubation with 10
641 μg/mL XBB.1.5 S2P protein and biotinylated SARS-CoV S2P at 4°C for 45 min. Afterwards,
642 the cells were washed again and incubated with a cocktail of flow cytometry and Hashtag
643 antibodies, consisting of CD3 PerCP-Cy5.5, CD19 APC/Cyanine 7, CD27 APC, IgM FITC,
644 anti-His PE/DazzleTM 594, Streptavidin BV421, and human Hashtag 3 at 4°C for 1 hour.
645 Stained cells were then washed, resuspended in RPMI 1640 complete medium, and sorted for
646 SARS-CoV and/or XBB.1.5 S2P trimer-specific memory B cells
647 (CD3−CD19+CD27+IgM−antigen+ live single lymphocytes) by flow cytometry. The sorted
648 cells were mixed with spike-in CD3+ cells and loaded into a 10X Chromium chip of the 5′
649 Single Cell Immune Profiling Assay (10X Genomics) at the Columbia University Single-Cell
650 Analysis Core. Library preparation and quality control were performed according to the
651 manufacturer's protocol and sequenced on a NextSeq 500 sequencer (Illumina).
652
653 **Identification of spike-specific antibody transcripts**
654 Antibody transcripts specific to the XBB.1.5 S2P spike and SARS-CoV spike trimers were
655 identified following previously established methods[38]. The assembly of full-length antibody
656 transcripts was performed utilizing the Cell Ranger V(D)J analysis software (version 3.1.0,
657 10X Genomics), employing default settings with the GRCh38 V(D)J germline sequence
658 version 2.0.0 as the reference genome. To differentiate between cells captured in the antigen-
659 specific sorting process and those added as spike-ins, the count module of Cell Ranger was
660 used to quantify the presence of all hashtag oligonucleotides in each cell based on Next
661 Generation Sequencing (NGS) raw data. Identification of high-confidence antigen-specific
662 cells was achieved using the following criteria: 1) A minimum of 100 copies of the antigen-
663 specific hashtag was required for a cell to be classified as antigen-specific, 2) Given that
664 hashtags might detach from their original cells and attach to others within the sample, a cell
665 was considered truly antigen-specific only if the copy number of its specific hashtag was at
666 least 1.5 times higher than that of any non-specific hashtag present, 3) Cells deemed to be of
667 low quality were excluded based on the cell quality assessment algorithm used by Cell Ranger,
668 4) Only cells expressing both productive heavy and light chain antibody gene pairs were
669 retained, 5) In instances where a cell exhibited more than two transcripts for heavy and/or light
670 chains, transcripts supported by fewer than three unique molecular identifiers (UMIs) were
671 discarded, and 6) Cells sharing identical heavy and light chain sequences, potentially indicative
672 of mRNA contamination, were consolidated into a single cell entry.
673
674 **Antibody transcript annotation**
675 Transcripts specific to the antigen were analyzed and annotated with SONAR version 2.0,
676 following previously established procedures. Assignment of V(D)J gene segments to each
677 transcript was conducted via BLASTn, employing specialized parameters against a germline
678 gene repository sourced from the International ImMunoGeneTics (IMGT) information system
679 database. The identification of the Complementarity Determining Region 3 (CDR3) utilized
680 BLAST alignments of the V and J segments, focusing on the conserved second cysteine within
681 the V segment and the WGXG (for heavy chains) or FGXG (for light chains) motifs in the J
682 segment, with "X" indicating any amino acid. Isotype determination for heavy chain transcripts
683 was achieved by analyzing Constant domain 1 (CH1) sequences against a human CH1 gene

684 database from IMGT, using BLASTn with standard parameters. The CH1 allele presenting the
685 lowest E-value was selected for precise isotype classification, adhering to a BLAST E-value
686 cutoff of 10e-6. Transcripts with incomplete V(D)J segments, frameshifts, or extraneous
687 sequences beyond the V(D)J region were discarded. The filtered transcripts were then aligned
688 to their corresponding germline V gene using CLUSTALO, and levels of somatic
689 hypermutation were quantified through the Sievers method. In instances where cells possessed
690 multiple high-quality heavy or light chains, potentially indicative of doublets, combinations of
691 all H and L chains were generated.
692
693 **Crystallization and Data processing**
694
695 19-77 Fab was produced by digestion of IgG with immobilized Endoproteinase Lys-C (Sigma
696 Aldrich) equilibrated with 25 mM Tris pH 8.5 and 1 mM EDTA for 3 h. The resulting Fab
697 was further purified from the cleaved Fc domain by cation exchange chromatography. Fab
698 purity was analyzed by SDS-PAGE and buffer-exchanged into 20 mM Tris, 150 mM, pH 7.4
699 prior to cryo-EM/Crystallization experiments.
700
701 19-77/SARS-CoV-2-RBD and 19-77/EG5.1-CoV-2-RBD complexes were prepared by mixing
702 each of the protein components at an equimolar concentration and incubating overnight at 4 °C.
703 Protein complexes were then isolated by gel filtration on a Superdex-200 column (Cytiva, GE
704 Healthcare). Fractions containing complexes were pooled and concentrated to 12.0 mg/mL in
705 SEC buffer. Screening for initial crystallization conditions was carried out in 96-well sitting
706 drop plates using the vapor-diffusion method with a Mosquito crystallization robot (TTP
707 LabTech) using various commercially available crystallization screens: MSCG-1 (Anthracene),
708 Proplex and LMB (Molecular dimensions). Diffraction quality crystals were obtained after
709 seven days in the following condition for 19-77/SARS-CoV-2-RBD: 0.1 M NaCl, 0.1 M Tris
710 pH 7.5, 12% w/v PEG 4000, and the following condition for 19-77/ EG5.1-CoV-2-RBD: 75%
711 MPD and 0.1 M HEPES pH 7.5.
712
713 Prior to data collection, crystals were cryoprotected with 40% ethylene glycol supplemented
714 in mother liquor and flash frozen in liquid nitrogen. X-ray diffraction data extending to 2.8 Å
715 (19-77/SARS-CoV-2-RBD) and 3.2 Å (19-77/ EG5.1-CoV-2-RBD) resolution were collected
716 at 100 K on beam line 17-ID-1 (AMX) at Brookhaven National Laboratory. Diffraction data
717 were processed with XDS[74] and scaled using AIMLESS[75] from the CCP4 software suite
718 (Collaborative Computational Project Number 4, 1994)[76]. Molecular replacement was
719 performed with PHASER[77], using a previously reported RBD structure (PDB 7L5B) and for
720 19-77 Fab, heavy chain (PDB 7XIK), light chain (3FIK) used as search models. Manual
721 rebuilding of the structure using COOT[78] was alternated with refinement using Phenix refine[79].
722 The Molprobity server was used for structure validation[80] and PyMOL (version 2.1,
723 Schrödinger, LLC) for structure visualization. A summary of the X-ray data collection and
724 refinement statistics are shown in **Extended Data Fig. 3c**.
725
726 **Cryo-EM sample preparation**

727 Fab fragments of antibodies were produced by digestion of IgG with immobilized
728 Endoproteinase Lys-C (Sigma-Aldrich) equilibrated with 25 mM Tris, pH 8.5, and 1 mM
729 EDTA for 3 h. The resulting Fabs were purified by ion-exchange chromatography on a mono-
730 Q column.
731
732 For the structure of 19-77 bound to D614G spike, the complex was made by mixing purified
733 SARS-CoV-2 S2P D614G spike protein with Fab in a 1:3 molar ratio (spike protomer:Fab) in
734 PBS, pH 7.4, such that the final concentration of spike was 1 mg/mL. This mixture was
735 incubated on ice for 1 h.
736
737 For the structures of the ternary complex of 19-77, RBDs, and S309, complexes were made by
738 mixing purified SARS-CoV-2 RBD with Fabs in a 1:1.2 molar ratio in PBS, pH 7.4, and further
739 purified using size exclusion chromatography (SEC) using a Superdex 200 Increase column.
740 The resulting complex peak was then concentrated to 4 mg/mL and held on ice until
741 vitrification.
742
743 Before freezing, 0.005% (w/v) n-Dodecyl β-D-maltoside (DDM) was added to deter preferred
744 orientation and aggregation during vitrification. Cryo-EM grids were prepared by applying 3
745 µL of sample to a freshly glow-discharged carbon-coated copper grid (CF 1.2/1.3 300 mesh);
746 the sample was then vitrified in liquid ethane using a Vitrobot Mark IV with a wait time of 30
747 s, a blot time of 3 s, and a blot force of 0.
748
749 **Cryo-EM data collection and analysis**
750 Cryo-EM data for single particle analysis were collected at the Columbia Cryo-EM Facility on
751 a Titan Krios electron microscope operating at 300 kV, equipped with a Gatan K3-BioQuantum
752 detector and energy filter, using the Leginon7 software package. Exposures were taken at a
753 magnification of 105,000x (pixel size of 0.83 Å), using a total electron flux of 58 e-/Å2
754 fractionated over 50 frames with an exposure time of 2.5 s. A random defocus range of -0.8 to
755 -2.0 µm was used.
756
757 Data processing was performed using cryoSPARC v3.3.1.8 Raw movies were aligned and
758 dose-weighted using patch motion correction, and the micrograph contrast transfer function
759 (CTF) parameters were estimated using patch CTF estimation. Micrographs were picked using
760 a blob or template picker and an initial particle set was selected using 2D classification. Further
761 heterogenous refinement was used to 3D-classify particles and remove debris. The resulting
762 curated particle sets were corrected for local motion and refined using homogenous refinement.
763 Local refinement was performed for the spike dataset using a mask enveloping the RBD+Fab
764 variable region. The default cryoSPARC auto-sharpened maps were then used to build the
765 models. Cryo-EM data collection and consensus refinements are summarized in **Extended**
766 **Data Fig. 3**.
767
768 **Model building and refinement**
769 Initial molecular models for Fabs were generated using Alphafold Multimer[81] using paired
770 heavy and light sequences. An RBD from PDB 7KNI, an RBD-up spike structure, was used

as a starting model. For the initial 19-77 structure, the 14-7 structure (PDB 8F89), RBD (PDB 8IOV), and S309 Fab (PDB 7XSW) were used. The initial models were rigid body docked into the density map using UCSF Chimera's "fit to map" tool and combined. The Fab CDR loops were manually fitted to the density map using Coot real space refinement. The models were fit to density using the ISOLDE package in ChimeraX[82]. Ramachandran outliers were corrected using ISOLDE's "flip peptide bond" feature. Real space refinement in Phenix[83] was performed to remove geometry outliers. The remaining manual adjustments were performed in Coot. Models were validated using MolProbity16 in Phenix and the PDB validation server and deposited to the PDB with accession codes: 19-77+SARS-CoV-2 D614G RBD (PDB 9CFE), 19-77+HK.3 RBD (PDB 9CFF), 19-77ΔV+HK.3 RBD (PDB 9CFG), and 19-77ΔV+JD.1.1 RBD (PDB 9CFH). A summary of data collection, processing, and model refinement statistics is shown in **Extended Data Fig. 3**.

***In silico* antibody engineering**

The energy changes for the binding of both the mutant and original 19-77 to the HK.3 RBD were calculated using FoldX software[40]. Initially, the 19-77 and HK.3 complex was repaired and optimized using the 'Optimize' function. Subsequently, every position in the heavy and light chains was subjected to saturation mutagenesis to all other amino acids using the 'BuildModel' function. This process generated both an unmutated model and a mutant model for each mutation. The binding energies were estimated with the 'AnalyseComplex' function, and the changes in Gibbs free energy (ΔΔG) were calculated based on the energy difference between each mutant and its corresponding original antibody-RBD complex.

Molecular dynamics analysis

Antibody 19-77, along with other VH3-53/66 class antibodies, was meticulously aligned through the RBD within each complex to ensure structural consistency. The R71A mutant antibodies were precisely engineered using the 'Mutagenesis' function in PyMOL version 2.5.4, provided by Schrödinger, LLC. Subsequently, the Fab regions of both the original and mutant antibodies underwent molecular dynamics simulations employing GROMACS on the WebGro server. The preprocessing was executed using the GROMOS96 54a7 force field and incorporated an SPC water model within a cubic simulation box, supplemented with 0.15M NaCl to mimic physiological ionic strength. The initial energy minimization step was set to 5000 iterations to stabilize the system. This was followed by equilibration and simulation phases under NVT/NPT conditions, conducted at a physiological temperature of 310K for 10 ns, with all other parameters set to default. To ensure the reliability of the simulation, the root-mean-square deviation (RMSD) of each system was manually monitored to verify that each simulation reached equilibrium. Additionally, the per-residue root-mean-square fluctuation (RMSF) analysis was conducted to assess the flexibility of residues within each Fab region.

Structure comparison analysis

The paratope and epitope residues for 19-77 was identified using PISA with the default parameters. The gene-specific substitution profiles (GSSP) for 19-77 germline genes were obtained from the cAb-Rep database (https://cab-rep.c2b2.columbia.edu/). The 19-77 and its mutant complexes were first superimposed by using the 'align' function in PyMOL 2.5.4. The

distance between the Cα from identical residues within the 19-77 heavy chains were then determined using the rms_cur function in PyMOL by in house python script.

Data analysis

IC_{50} values were determined by fitting the data to five-parameter dose-response curves in GraphPad Prism v.10.3. GraphPad Prism v.10.3 was also used for data visualization. PISA was used for identifying antibody-spike interface residuals. PyMOL V.2.5.4 was used to perform mutagenesis and to generate structural plots.

Data availability

All experimental data are provided in this manuscript. SARS-CoV-2 spike sequences were sourced from the Global Initiative on Sharing All Influenza Data (GISAID) database (https://www.gisaid.org/). The sequences for 19-77 and 19-79 are deposited in NCBI under accession: PV010127 to PV010130 [https://www.ncbi.nlm.nih.gov/nuccore/PV010127,PV010128,PV010129,PV010130]. Structures are available in the Protein Data Bank (PDB) under the following IDs: 9CFE [https://www.rcsb.org/structure/9CFE], 9CFF [https://www.rcsb.org/structure/9CFF], 9CFG [https://www.rcsb.org/structure/9CFG], 9CFH [https://www.rcsb.org/structure/9CFH], and 9CAV [https://www.rcsb.org/structure/9CAV]. All data supporting the results of this study are available in the article, supplementary, and source data files. Source Data are provided with this paper.

References

1. Wang, P. et al. Antibody resistance of SARS-CoV-2 variants B.1.351 and B.1.1.7. *Nature* **593**, 130-135 (2021).
2. Cerutti, G. et al. Potent SARS-CoV-2 neutralizing antibodies directed against spike N-terminal domain target a single supersite. *Cell Host Microbe* **29**, 819-833 e817 (2021).
3. McCallum, M. et al. N-terminal domain antigenic mapping reveals a site of vulnerability for SARS-CoV-2. *Cell* **184**, 2332-2347 e2316 (2021).
4. Wang, P. et al. Increased resistance of SARS-CoV-2 variant P.1 to antibody neutralization. *Cell Host Microbe* **29**, 747-751 e744 (2021).
5. Barnes, C.O. et al. SARS-CoV-2 neutralizing antibody structures inform therapeutic strategies. *Nature* **588**, 682-687 (2020).
6. Planas, D. et al. Reduced sensitivity of SARS-CoV-2 variant Delta to antibody neutralization. *Nature* **596**, 276-280 (2021).
7. Shi, R. et al. A human neutralizing antibody targets the receptor-binding site of SARS-CoV-2. *Nature* **584**, 120-124 (2020).
8. Jones, B.E. et al. The neutralizing antibody, LY-CoV555, protects against SARS-CoV-2 infection in nonhuman primates. *Sci Transl Med* **13** (2021).
9. Hansen, J. et al. Studies in humanized mice and convalescent humans yield a SARS-CoV-2 antibody cocktail. *Science* **369**, 1010-1014 (2020).
10. Park, Y.J. et al. Antibody-mediated broad sarbecovirus neutralization through ACE2 molecular mimicry. *Science* **375**, 449-454 (2022).
11. Shu, Y. & McCauley, J. GISAID: Global initiative on sharing all influenza data - from vision to reality. *Euro Surveill* **22** (2017).
12. Scott, L. et al. Track Omicron's spread with molecular data. *Science* **374**, 1454-1455 (2021).
13. Liu, L. et al. Striking antibody evasion manifested by the Omicron variant of SARS-CoV-2. *Nature* **602**, 676-681 (2022).
14. Carreno, J.M. et al. Activity of convalescent and vaccine serum against SARS-CoV-2 Omicron. *Nature* **602**, 682-688 (2022).
15. Cameroni, E. et al. Broadly neutralizing antibodies overcome SARS-CoV-2 Omicron antigenic shift. *Nature* **602**, 664-670 (2022).
16. Planas, D. et al. Considerable escape of SARS-CoV-2 Omicron to antibody neutralization. *Nature* **602**, 671-675 (2022).
17. Cao, Y. et al. Omicron escapes the majority of existing SARS-CoV-2 neutralizing antibodies. *Nature* **602**, 657-663 (2022).
18. Cele, S. et al. Omicron extensively but incompletely escapes Pfizer BNT162b2 neutralization. *Nature* **602**, 654-656 (2022).
19. Zost, S.J. et al. Potently neutralizing and protective human antibodies against SARS-CoV-2. *Nature* **584**, 443-449 (2020).
20. Wang, Q. et al. Antibody evasion by SARS-CoV-2 Omicron subvariants BA.2.12.1, BA.4 and BA.5. *Nature* **608**, 603-608 (2022).
21. Wang, Q. et al. Alarming antibody evasion properties of rising SARS-CoV-2 BQ and XBB subvariants. *Cell* **186**, 279-286 e278 (2023).
22. Pinto, D. et al. Cross-neutralization of SARS-CoV-2 by a human monoclonal SARS-CoV antibody. *Nature* **583**, 290-295 (2020).
23. Westendorf, K. et al. LY-CoV1404 (bebtelovimab) potently neutralizes SARS-CoV-2 variants. *Cell Rep* **39**, 110812 (2022).

24. Wang, Q. et al. Antibody neutralisation of emerging SARS-CoV-2 subvariants: EG.5.1 and XBC.1.6. *Lancet Infect Dis* **23**, e397-e398 (2023).
25. Yue, C. et al. ACE2 binding and antibody evasion in enhanced transmissibility of XBB.1.5. *Lancet Infect Dis* **23**, 278-280 (2023).
26. Jian, F. et al. Convergent evolution of SARS-CoV-2 XBB lineages on receptor-binding domain 455-456 synergistically enhances antibody evasion and ACE2 binding. *PLoS Pathog* **19**, e1011868 (2023).
27. Wang, Q. et al. Antigenicity and receptor affinity of SARS-CoV-2 BA.2.86 spike. *Nature* (2023).
28. Hong, Q. et al. Molecular basis of receptor binding and antibody neutralization of Omicron. *Nature* **604**, 546-552 (2022).
29. Guenthoer, J. et al. Identification of broad, potent antibodies to functionally constrained regions of SARS-CoV-2 spike following a breakthrough infection. *Proc Natl Acad Sci U S A* **120**, e2220948120 (2023).
30. Liu, L. et al. Antibodies targeting a quaternary site on SARS-CoV-2 spike glycoprotein prevent viral receptor engagement by conformational locking. *Immunity* **56**, 2442-2455 e2448 (2023).
31. Looi, M.K. Covid-19: WHO adds JN.1 as new variant of interest. *BMJ* **383**, 2975 (2023).
32. Wang, Q. et al. XBB.1.5 monovalent mRNA vaccine booster elicits robust neutralizing antibodies against XBB subvariants and JN.1. *Cell Host Microbe* **32**, 315-321 e313 (2024).
33. FDA (2024).
34. Wang, Q. et al. Antibody evasiveness of SARS-CoV-2 subvariants KP.3.1.1 and XEC. *bioRxiv*, 2024.2011.2017.624037 (2024).
35. Wang, Q., Guo, Y., Ho, J. & Ho, D.D. Activity of Research-Grade Pemivibart against Recent SARS-CoV-2 JN.1 Sublineages. *N Engl J Med* **391**, 1863-1864 (2024).
36. Wang, Q. et al. Antibody evasiveness of SARS-CoV-2 subvariants KP.3.1.1 and XEC. *Cell Rep* **44**, 115543 (2025).
37. Cai, Y. et al. AZD3152 neutralizes SARS-CoV-2 historical and contemporary variants and is protective in hamsters and well tolerated in adults. *Sci Transl Med* **16**, eado2817 (2024).
38. Liu, L. et al. Potent neutralizing antibodies against multiple epitopes on SARS-CoV-2 spike. *Nature* **584**, 450-456 (2020).
39. Yuan, M. et al. Structural basis of a shared antibody response to SARS-CoV-2. *Science* **369**, 1119-1123 (2020).
40. Schymkowitz, J. et al. The FoldX web server: an online force field. *Nucleic Acids Res* **33**, W382-388 (2005).
41. Fenwick, C. et al. Broadly potent anti-SARS-CoV-2 antibody shares 93% of epitope with ACE2 and provides full protection in monkeys. *J Infect* **87**, 524-537 (2023).
42. Cao, Y. et al. Imprinted SARS-CoV-2 humoral immunity induces convergent Omicron RBD evolution. *Nature* (2022).
43. Nutalai, R. et al. Potent cross-reactive antibodies following Omicron breakthrough in vaccinees. *Cell* **185**, 2116-2131 e2118 (2022).
44. Cao, Y. et al. Potent Neutralizing Antibodies against SARS-CoV-2 Identified by High-Throughput Single-Cell Sequencing of Convalescent Patients' B Cells. *Cell* **182**, 73-84 e16 (2020).
45. Cao, Y. et al. Rational identification of potent and broad sarbecovirus-neutralizing antibody cocktails from SARS convalescents. *Cell Rep* **41**, 111845 (2022).

46. Jian, F. et al. A generalized framework to identify SARS-CoV-2 broadly neutralizing antibodies. *bioRxiv*, 2024.2004.2016.589454 (2024).
47. Rosen, L.E. et al. A potent pan-sarbecovirus neutralizing antibody resilient to epitope diversification. *Cell* (2024).
48. Yu, L. et al. Potent and broadly neutralizing antibodies against sarbecoviruses elicited by single ancestral SARS-CoV-2 infection. *bioRxiv*, 2024.2006.2006.597720 (2024).
49. Yao, T., Ma, Z., Lan, K., Guo, Y. & Liu, L. Neutralizing Activity and Viral Escape of Pemivibart by SARS-CoV-2 JN.1 sublineages. *bioRxiv*, 2024.2011.2008.622746 (2024).
50. Planas, D. et al. Escape of SARS-CoV-2 Variants KP.1.1, LB.1, and KP3.3 From Approved Monoclonal Antibodies. *Pathog Immun* **10**, 1-11 (2024).
51. Tixagevimab and Cilgavimab (Evusheld) for Pre-Exposure Prophylaxis of COVID-19. *JAMA* **327**, 384-385 (2022).
52. FDA (2024).
53. Casadevall, A. & Focosi, D. Lessons from the Use of Monoclonal Antibodies to SARS-CoV-2 Spike Protein During the COVID-19 Pandemic. *Annu Rev Med* **76**, 1-12 (2025).
54. Casadevall, A. & Focosi, D. Anti-Spike Monoclonal Antibody Monotherapies and Immune Escape Risk Minimization Strategies. *Clin Infect Dis* **80**, 484-485 (2025).
55. Marks, J.D. et al. By-passing immunization: building high affinity human antibodies by chain shuffling. *Biotechnology (N Y)* **10**, 779-783 (1992).
56. Yoshinaga, K. et al. Ig L-chain shuffling for affinity maturation of phage library-derived human anti-human MCP-1 antibody blocking its chemotactic activity. *J Biochem* **143**, 593-601 (2008).
57. Kim, H.Y., Stojadinovic, A. & Izadjoo, M.J. Affinity maturation of monoclonal antibodies by multi-site-directed mutagenesis. *Methods Mol Biol* **1131**, 407-420 (2014).
58. Banach, B.B. et al. Antibody-directed evolution reveals a mechanism for enhanced neutralization at the HIV-1 fusion peptide site. *Nat Commun* **14**, 7593 (2023).
59. Pan, Y. et al. Screening of potent neutralizing antibodies against SARS-CoV-2 using convalescent patients-derived phage-display libraries. *Cell Discov* **7**, 57 (2021).
60. Hess, G.T. et al. Directed evolution using dCas9-targeted somatic hypermutation in mammalian cells. *Nat Methods* **13**, 1036-1042 (2016).
61. Mason, D.M. et al. High-throughput antibody engineering in mammalian cells by CRISPR/Cas9-mediated homology-directed mutagenesis. *Nucleic Acids Res* **46**, 7436-7449 (2018).
62. Wellner, A. et al. Rapid generation of potent antibodies by autonomous hypermutation in yeast. *Nat Chem Biol* **17**, 1057-1064 (2021).
63. Desautels, T.A. et al. Computationally restoring the potency of a clinical antibody against Omicron. *Nature* **629**, 878-885 (2024).
64. Shan, S. et al. Deep learning guided optimization of human antibody against SARS-CoV-2 variants with broad neutralization. *Proc Natl Acad Sci U S A* **119**, e2122954119 (2022).
65. Li, L. et al. Machine learning optimization of candidate antibody yields highly diverse sub-nanomolar affinity antibody libraries. *Nat Commun* **14**, 3454 (2023).
66. Burn Aschner, C. et al. A multi-specific, multi-affinity antibody platform neutralizes sarbecoviruses and confers protection against SARS-CoV-2 in vivo. *Sci Transl Med* **15**, eadf4549 (2023).

67. Song, R., Oren, D.A., Franco, D., Seaman, M.S. & Ho, D.D. Strategic addition of an N-linked glycan to a monoclonal antibody improves its HIV-1-neutralizing activity. *Nat Biotechnol* **31**, 1047-1052 (2013).
68. Ovchinnikov, V., Louveau, J.E., Barton, J.P., Karplus, M. & Chakraborty, A.K. Role of framework mutations and antibody flexibility in the evolution of broadly neutralizing antibodies. *Elife* **7** (2018).
69. Tramontano, A., Chothia, C. & Lesk, A.M. Framework residue 71 is a major determinant of the position and conformation of the second hypervariable region in the VH domains of immunoglobulins. *J Mol Biol* **215**, 175-182 (1990).
70. Yanaka, S., Moriwaki, Y., Tsumoto, K. & Sugase, K. Elucidation of potential sites for antibody engineering by fluctuation editing. *Sci Rep* **7**, 9597 (2017).
71. Liu, L. et al. An antibody class with a common CDRH3 motif broadly neutralizes sarbecoviruses. *Sci Transl Med* **14**, eabn6859 (2022).
72. Hsieh, C.L. et al. Structure-based design of prefusion-stabilized SARS-CoV-2 spikes. *Science* **369**, 1501-1505 (2020).
73. Chan, K.K. et al. Engineering human ACE2 to optimize binding to the spike protein of SARS coronavirus 2. *Science* **369**, 1261-1265 (2020).
74. Kabsch, W. Integration, scaling, space-group assignment and post-refinement. *Acta Crystallogr D Biol Crystallogr* **66**, 133-144 (2010).
75. Evans, P.R. & Murshudov, G.N. How good are my data and what is the resolution? *Acta Crystallogr D Biol Crystallogr* **69**, 1204-1214 (2013).
76. Winn, M.D. et al. Overview of the CCP4 suite and current developments. *Acta Crystallogr D Biol Crystallogr* **67**, 235-242 (2011).
77. McCoy, A.J. Solving structures of protein complexes by molecular replacement with Phaser. *Acta Crystallogr D Biol Crystallogr* **63**, 32-41 (2007).
78. Emsley, P. & Cowtan, K. Coot: model-building tools for molecular graphics. *Acta Crystallogr D Biol Crystallogr* **60**, 2126-2132 (2004).
79. Adams, P.D. et al. PHENIX: a comprehensive Python-based system for macromolecular structure solution. *Acta Crystallogr D Biol Crystallogr* **66**, 213-221 (2010).
80. Davis, I.W., Murray, L.W., Richardson, J.S. & Richardson, D.C. MOLPROBITY: structure validation and all-atom contact analysis for nucleic acids and their complexes. *Nucleic Acids Res* **32**, W615-619 (2004).
81. Jumper, J. et al. Highly accurate protein structure prediction with AlphaFold. *Nature* **596**, 583-589 (2021).
82. Meng, E.C. et al. UCSF ChimeraX: Tools for structure building and analysis. *Protein Sci* **32**, e4792 (2023).
83. Liebschner, D. et al. Macromolecular structure determination using X-rays, neutrons and electrons: recent developments in Phenix. *Acta Crystallogr D Struct Biol* **75**, 861-877 (2019).

1024 **Acknowledgements**
1025 This study was supported by funding from the Gates Foundation (INV019355) and donations
1026 from Andrew and Peggy Cherng.
1027
1028 **Contributions**
1029 D.D.H. and L.L. conceived this project. J.Y. J.H., and C.C.T. constructed antibody expression
1030 plasmids. R.G.C. conducted cryo-EM and E.R.R. conducted x-ray. J.Y. studied antibody PK
1031 in mice. M.S.N. and Y.H. performed escape virus selection on live virus. Y.G. did
1032 bioinformatic and structural analyses. Q.W., I.A.M., M.W., H.H., C.C.T. and L.L. conducted
1033 pseudovirus neutralization assays. Q.W. and L.L. conducted all other experiments including
1034 antigen-specific B cell sorting, protein expression plasmid construction, ELISA,
1035 protein/antibody purification, rVSV-JN.1 escape variants selection, etc. L.S., L.L. and D.D.H.
1036 directed and supervised the project. Q.W., Y.G., R.G.C., L.L., L.S., and D.D.H. analyzed the
1037 results and wrote the manuscript.
1038
1039 **Competing interests**
1040 Q.W., J.Y., R.G.C. Y.G., L.S., L.L., and D.D.H. are inventors on the patent application (WH
1041 Ref: 0019240.01338US1) or the provisional patent application (63/619,716) filed by Columbia
1042 University for a number of SARS-CoV-2 neutralizing antibodies described in this manuscript.
1043 Both sets of applications are under review. D.D.H. is a co-founder of TaiMed Biologics and
1044 RenBio, consultant to WuXi Biologics and Brii Biosciences, and board director for Vicarious
1045 Surgical. The remaining authors declare no competing interests.